Air Induced Formation of $Cs_3Bi_2Br_9$/Cs_3BiBr_6 Bulk Heterojunction and Its Dual-band Photodetection Abilities for Light Communication

Fa Cao, Ziqing Li, Xinya Liu, Zhifeng Shi,* and Xiaosheng Fang*

Metal-halide perovskites have long carrier diffusion lengths, low trap densities, and high carrier mobilities, and are therefore of value in the development of photodetectors (PDs). However, the research on dual-band lead-free perovskite bulk heterojunction has not been well developed. Here, a novel air induced formation of $Cs_3Bi_2Br_9$/Cs_3BiBr_6 bulk heterojunction, reaching a high-performance dual-band photodetecting performance with a UV main band (360 nm) peak responsivity of 5.6 mA W^{-1} and a blue sub-band (450 nm) peak responsivity of 0.6 mA W^{-1} at 2 V, is reported. The bulk heterojunction exhibits superior photodetecting performance than that of lateral heterojunction. Furthermore, the PD exhibits a fast response speed (rise time 1.4 µs and decay time 2.0 µs) and good cyclic stability. Theoretical and experimental characterizations suggest $Cs_3Bi_2Br_9$ exhibits a more stable structure in air than that of Cs_3BiBr_6. The dual-band photodetection abilities of $Cs_3Bi_2Br_9$/Cs_3BiBr_6 bulk-heterojunction demonstrate great application prospects in light communication. These state-of-the-art findings shed light on the fabrication of novel dual-band high-performance PDs based on lead-free perovskite bulk-heterojunction.

1. Introduction

Metal halide perovskite-based crystals have emerged as a new category of optoelectronic materials for the applications of solar cells, light-emitting diodes, photodetectors (PDs), etc.,[1–3] due

F. Cao, X. Liu, X. Fang
Department of Materials Science
Fudan University
Shanghai 200433, P. R. China
E-mail: xshfang@fudan.edu.cn
F. Cao
Zhangjiang Fudan International Innovation Center
Shanghai 201210, P. R. China
Z. Li, X. Fang
Institute of Optoelectronics
Fudan University
Shanghai 200433, P. R. China
Z. Shi
Key Laboratory of Materials Physics of Ministry of Education
School of Physics and Microelectronics
Zhengzhou University
Daxue Road 75, Zhengzhou 450052, P. R. China
E-mail: shizf@zzu.edu.cn

The ORCID identification number(s) for the author(s) of this article can be found under https://doi.org/10.1002/adfm.202206151.

DOI: 10.1002/adfm.202206151

to their prominent optoelectronic properties including high carrier mobility, long carrier diffusion length, and large light absorption coefficient.[4,5] However, the previous studies are mostly based on reports of single-phase perovskites, which can only absorb or respond to a specific wavelength.[6,7] With the development of modern society, broad-band or dual-band response devices have attracted much attention.[8–10] Recent reports demonstrated that wide band achromatic retardation in the visible and near-infrared (532–800 nm) regions for Cs_4PbBr_6 perovskite crystals embedded with $CsPbBr_3$,[4] which aroused our interest to design perovskite bulk heterojunction for dual-band PDs, since their great application prospect in optical communication.[8,11] Even the highly narrow-band dual-band PDs based on $(C_4H_9NH_3)_2PbI_4$/$(C_4H_9NH_3)_2(CH_3NH_3)Pb_2I_7$ have been reported,[4] however, toxic Pb inhibit the development of lead halide perovskite.[12] PDs composed of non-toxic Cs_2SnI_6 perovskite/ZnO heterojunction demonstrate voltage-switched dual-band photodetecting abilities, however, lattice and thermal mismatch should be overcome during the epitaxial growth of different semiconductor layers.[12] Using a dual-band optical signal as the receptor can achieve the encryption of information. In the process of optical signal coding, the dual-band optical signal is modulated in different forms. The PD will lead to wrong decoding if it can only identify monochromatic light signals. Therefore, it is urgent to explore lead-free, environmental-friendly, and highly stable perovskites with outstanding optoelectronic performance by simple methods.[13]

Very recently, cesium bismuth bromide ($Cs_3Bi_yBr_{3+3y}$; $y = 1,2$), an emerging all-inorganic lead-free halide material system, has been confirmed to possess high quantum efficiency and excellent air stability.[14–18] The photodetection properties of $Cs_3Bi_2Br_9$ (direct bandgap $\approx$2.6 eV) have been studied by combining it with various other semiconductors, which exhibit superior photodetection performances.[16] However, there is no report regarding dual-band photodetection PDs based on $Cs_3Bi_yBr_{3+3y}$. Interestingly, it is reported recently that Cs_3BiBr_6 (direct bandgap 3.2–3.4 eV) exhibits different energy bandgaps with $Cs_3Bi_2Br_9$,[17] while they have the same constituent elements and preparation methods, therefore, it is feasible to prepare $Cs_3Bi_2Br_9$/Cs_3BiBr_6 (CBB) bulk heterojunction in one

step by controlling the phase evolution of Cs_3BiBr_6 to $Cs_3Bi_2Br_9$ as the transformation of Cs_4PbBr_6 to $CsPbBr_3$ [17] and realize potential dual-band photodetection performances. Even the thin solid film of Cs_3BiBr_6 and $Cs_3Bi_2Br_9$ has been investigated, however, there is no report about their bulk heterojunction. And the methods to control the evolution of Cs_3BiBr_6 to $Cs_3Bi_2Br_9$ are still lacking.[14]

In this study, for the first time, we observed and characterized a novel air induced the formation of CBB bulk heterojunction. Theoretical and experimental characterization suggest that $Cs_3Bi_2Br_9$ exhibits a more stable structure in air. Furthermore, the CBB perovskite bulk heterojunction exhibits a high-performance dual-band photodetecting performance with a UV main band (360 nm) peak responsivity of 5.6 mA W^{-1} and a blue sub-band (450 nm) peak responsivity of 0.6 mA W^{-1} at 2 V, demonstrating great application prospects in light communication. Our findings open a new way of designing lead-free perovskite bulk heterojunction for more than one band photodetection.

2. Results and Discussion

The fabrication process of the CBB bulk heterojunction is shown in **Figure 1**a. Figure 1b illustrates the optical microscopic images of the as-grown Cs_3BiBr_6(DMSO) and CBB micro-ribbons (MRs) on the substrates of covered glass at different stages. At the early growth stage, the Cs_3BiBr_6(DMSO) MRs nucleate and grow in DMSO solution (45 and 68 h) (white circled). When the growth time is further increased to 72 and 78 h, the end of Cs_3BiBr_6(DMSO) MRs exposed to the air gradually evolves into a sawtooth shape, and the $Cs_3Bi_2Br_9$

phase is formed (red circled). The air induced the transformation of Cs_3BiBr_6 to $Cs_3Bi_2Br_9$ phase may own to the reason that the single point energy of $Cs_3Bi_2Br_9$ is −27633.69 eV which is lower than that of Cs_3BiBr_6(DMSO) (−27627.38 eV), demonstrating its higher air-stable structure of $Cs_3Bi_2Br_9$, as shown in Figure 1c. With the time increased to 90 and 99 h, the surface of Cs_3BiBr_6(DMSO) MRs is completely covered by $Cs_3Bi_2Br_9$. The central zone and edge demarcation lines are clearly visible. The CBB MRs have ribbon-like structures with a length of ≈1 mm and a width ranging from tens to 200 microns. The edge height of the MR is 3 μm and the middle height is 4.2 μm, as shown in the inset of Figure 1b (99 h) The calculated volume ratio of Cs_3BiBr_6 to $Cs_3Bi_2Br_9$ is ≈0.415.

To fabricate pure Cs_3BiBr_6 MRs, we uncovered the glass at the early stage of the preparation process(≈20 h). However, the surface of Cs_3BiBr_6(DMSO) MRs immediately evolved into $Cs_3Bi_2Br_9$ and some of the Cs_3BiBr_6(DMSO) MRs disappeared, as proved by Figures S1 and S2 (Supporting Information), demonstrating that Cs_3BiBr_6(DMSO) MRs are unstable in air.

The X-ray diffraction (XRD) pattern is displayed in **Figure 2**a. The main diffraction peaks with 2θ of 12.90°, 18.15°, 25.93°, 27.14°, 32.31°, 39.29°, 46.07°, 56.04°, 67.60°, and 77.78° are indexed to the (100), (002), (200), (003), (202), (104), (005), (006), (007), and (008) crystal facets of the hexagonal-phase $Cs_3Bi_2Br_9$ (JCPDS # 44–0714). A weak peak centered at 19.36° is ascribed to the (202) crystal facets of Cs_3BiBr_6 (space group: p1) as calculated by VESTA software. The X-ray photoelectron spectroscopy (XPS) measurements were further performed to confirm the valence state and the element distribution of CBB. The full XPS spectrum (Figure S3, Supporting Information) demonstrates that no impurity elements can be observed except the chemical
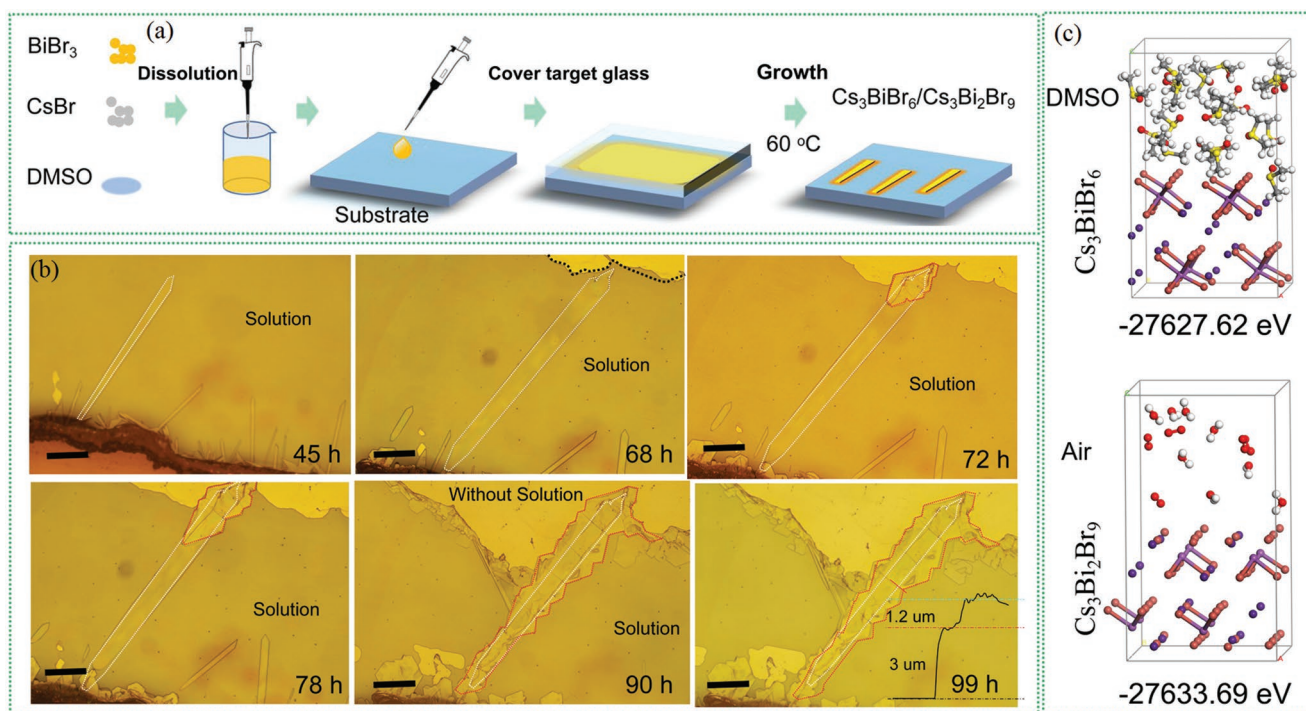
Figure 1. a) The fabrication process of CBB MRs. b) In-situ observation of Cs_3BiBr_6(DMSO) (white circled) embedded in $Cs_3Bi_2Br_9$ (red circled) (scale bar 200 μm). c) Atomic models of Cs_3BiBr_6 in DMSO and $Cs_3Bi_2Br_9$ in air. And their single point energy in stable condition.
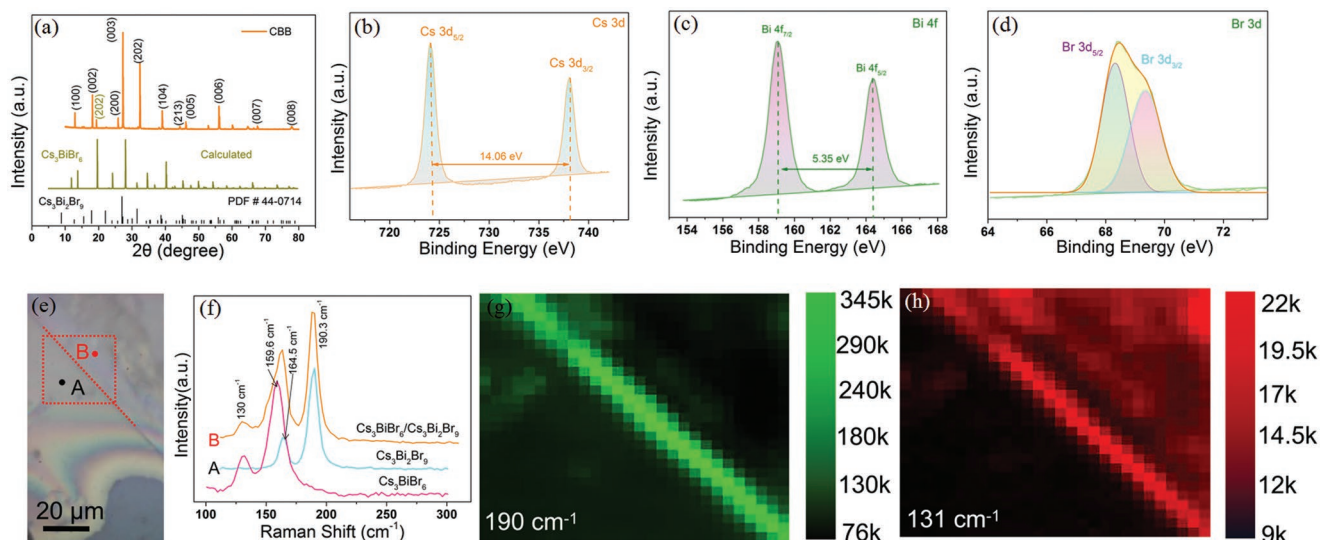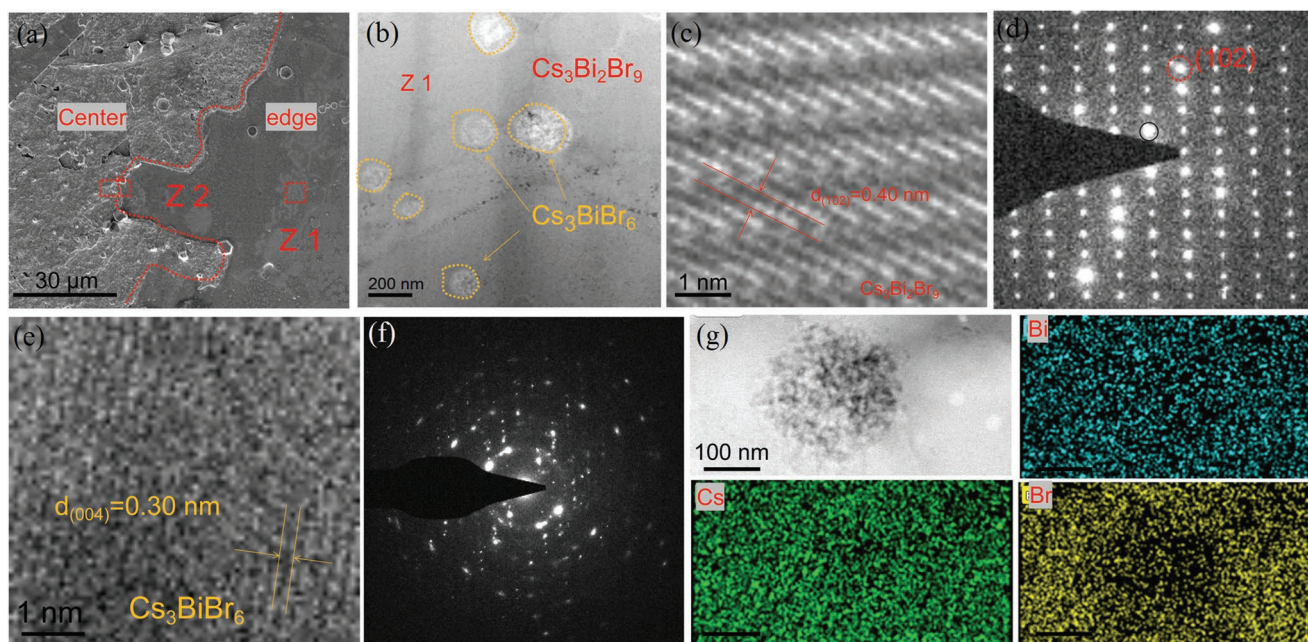
Figure 2. a) XRD pattern of CBB and calculated XRD patterns of Cs_3BiBr_6 by vesta. b–d) XPS spectra of Cs 3d, Bi 4f, and Br 3d, respectively. e) Optical image of the CBB and $Cs_3Bi_2Br_9$ interface. f) Raman spectra of $Cs_3Bi_2Br_9$ and CBB corresponding to (e). g,h) Raman mapping of $Cs_3Bi_2Br_9$ and Cs_3BiBr_6.

absorbed C and O elements. Furthermore, we could observe the signals of Cs ($3d_{5/2}$, $3d_{3/2}$, separated spin-orbital components $D = 14.06$ eV), Bi ($4f_{7/2}$, $4f_{5/2}$, $D = 5.35$ eV) and Br ($3d_{5/2}$, $3d_{3/2}$, $D = 1.0$ eV), indicating their valence (+1, +3, and −1, respectively), which are consistent with the formula and confirm the existence of all elements in this material (Figure 2b–d).[19] To further determine the phase of the center and middle of the MRs, the Raman microanalysis was performed and the corresponding results are shown in Figure 2e–h. Peaks at 190.3 cm^{-1} and 164.5 cm^{-1} agree closely with the Raman spectrum from the $Cs_3Bi_2Br_9$, corresponding to the A_{1g} and E_g normal modes of Bi-Br vibrations, while two peaks centered at 159.6 and 130 cm^{-1} are ascribed to Cs_3BiBr_6 (Figure 2f).[14] From the Raman mapping results, we could further confirm that the edge of the MRs is mainly composed of $Cs_3Bi_2Br_9$ and the center is made up of Cs_3BiBr_6 and $Cs_3Bi_2Br_9$ mixed phase (Figure 2g,h).

A detailed local investigation of the structural morphology and the chemical composition of the CBB MRs bulk-heterojunction is presented in **Figure 3** by scanning electron microscopy (SEM), transmission electron microscopy (TEM), and high-resolution TEM (HRTEM) imaging, energy dispersive X-ray spectroscopy (EDS) mapping, respectively. The SEM image (Figure 3a) shows that the CBB MRs have a rough center and smooth edges. And the corresponding root mean square (R_q) of the edge and center are 9.3 and 1.2 nm, respectively (Figure S4, Supporting Information). To learn more about the micro-structure of the CBB MRs, the cross-section TEM images corresponding to zone 1 (Z1) and zone 2 (Z2) are investigated. Figure 3b is the cross-section TEM image of Z1 and Figure 3c,e is the HRTEM images corresponding to the outside and inside of the yellow circled areas (Figure 3b), respectively. The interlayer spacing of 0.40 nm (Figure 3c) is in good agreement with the d spacing of hexagonal $Cs_3Bi_2Br_9$ (102) planes and the selected area electron diffraction (SAED) pattern (Figure 3d), demonstrating the single crystal nature of $Cs_3Bi_2Br_9$. While the d spacing of 0.30 nm (Figure 3e) can be attributed to (004)

planes of polycrystalline Cs_3BiBr_6 (demonstrated by the SAED pattern of Figure 3f). The elemental mapping images of Cs, Bi, and Br in Figure 3g further prove that the Cs_3BiBr_6 nanodots are embedded in a single crystal $Cs_3Bi_2Br_9$, which formed the bulk-heterojunction. The cross-section TEM and HRTEM images of Z2 are illustrated in Figure S5 (Supporting Information), demonstrating the formation of lateral heterojunction.

Based on the above experiments and characterizations, we propose the mechanisms of air induced CBB bulk heterojunction, as shown in **Figure 4**a. The Cs_3BiBr_6(DMSO) MRs nucleate and grow in DMSO solution at the early stage (Step 1).[20] When the one end of Cs_3BiBr_6(DMSO) MRs exposed to the air, the $Cs_3Bi_2Br_9$ with a sawtooth shape is formed (Step 2). Figure 4b illustrates the change of crystal structure from Cs_3BiBr_6(DMSO) to $Cs_3Bi_2Br_9$ at the DMSO/air interface. The transformation process can be written as $Cs_3BiBr_6(DMSO) + BiBr_3 \xrightarrow{60°C+Air} Cs_3Bi_2Br_9(Air)$, which is consistent with the above results.[15] Figure S6a–c shows (Supporting Information) the single point energy of Cs_3BiBr_6 in DMSO, DMSO/air (O_2 and H_2O), and air, respectively, and Figure S6d,e (Supporting Information) demonstrates the single point energy of $Cs_3Bi_2Br_9$ in DMSO/air and air, respectively. The lower the single point energy of Cs_3BiBr_6 and $Cs_3Bi_2Br_9$, the higher the stability of the structure. In view of the single point energy, Cs_3BiBr_6 is more stable in DMSO solution than in the air, which is consistent with the experimental phenomenon we observed and the ever reported.[20] After the $Cs_3Bi_2Br_9$ is formed, it will grow epitaxially along the H and P direction in DMSO solution (Step 3). And the red circled area will stop growing when there is no DMSO solution. The corresponding cross-section growth diagram is shown in Figure 4c. While the $Cs_3Bi_2Br_9$ grows epitaxially along the P direction, the Cs_3BiBr_6 nanodot formed in the DMSO solution will be embedded in a single crystal $Cs_3Bi_2Br_9$. And the $Cs_3BiBr_6/Cs_3Bi_2Br_9$ bulk heterojunction formed, which can be proved by the TEM results in Figure 3b.

**ADVANCED
SCIENCE NEWS**

www.advancedsciencenews.com

**ADVANCED
FUNCTIONAL
MATERIALS**

www.afm-journal.de

**Figure 3.** a) SEM image of the CBB and $Cs_3Bi_2Br_9$ interface. b) Cross-section TEM image corresponding zone 1 (Z1) in (a). c,e) HRTEM image of outside and inside yellow circled area corresponding to (b), respectively. d,f) the corresponding SAED patterns corresponding to (c) and (e), respectively. g) EDS mappings of a single Cs_3BiBr_6 nanodot embedded in $Cs_3Bi_2Br_9$.

To investigate the photodetecting ability of the CBB MRs, three types of PDs are fabricated, as shown in **Figure 5**a. The photoelectric properties of the PD1 (center of the CBB MRs, mainly composed of Cs_3BiBr_6), PD2 (Lateral heterojunction), and PD3 (Bulk heterojunction) were investigated in ambient conditions by using two-probe methods, and the corresponding current-voltage ($I–V$) curves are shown in Figure 5b–d,

respectively. The approximately linear behavior of the $I–V$ curves (Figure S7, Supporting Information) demonstrates its good ohmic contact. It is clear that the three types of PD exhibit almost the same ultra-low dark current (10^{-13} A) at 2 V bias, however, PD3 shows the highest photocurrent under both UV (10^{-10} A) and blue light (10^{-11} A) illumination, which may be attributed to the less defects of the single crystal in Z1 area
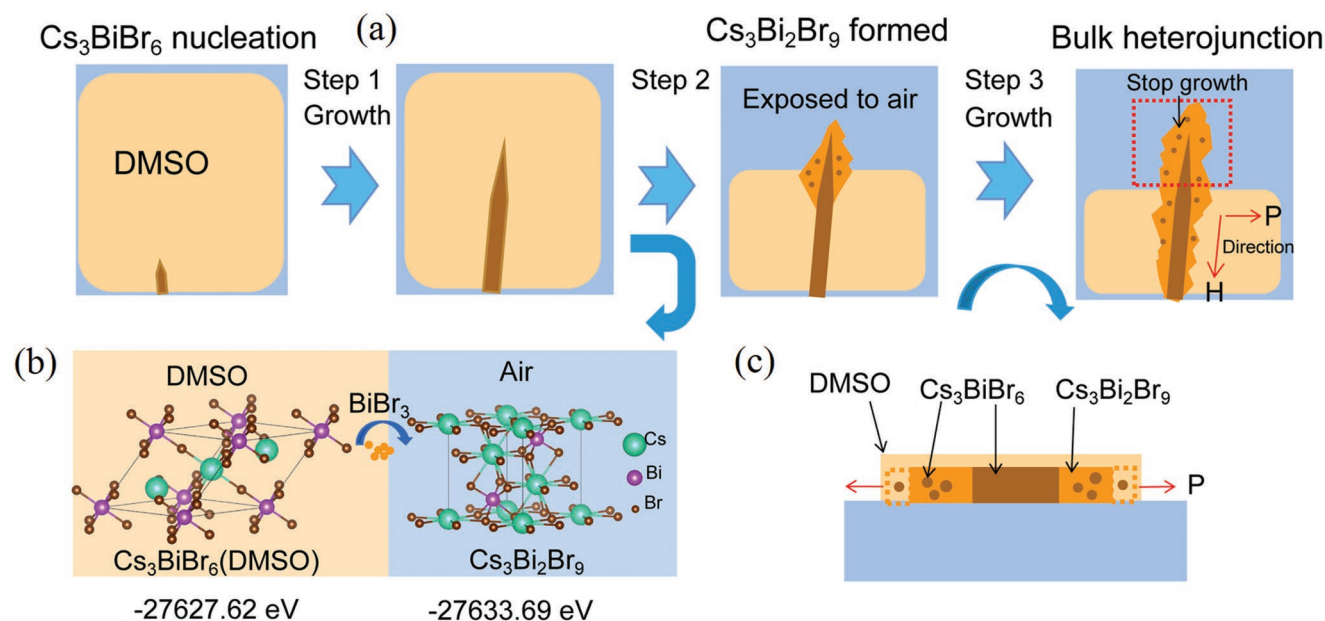
Figure 4. a) Schematic diagram of the evolution of Cs_3BiBr_6 to $Cs_3Bi_2Br_9$. b) Schematic illustration of crystal structure change and transformation process from Cs_3BiBr_6 to $Cs_3Bi_2Br_9$ when exposed to air. c) Schematic diagram of bulk heterojunction formation.
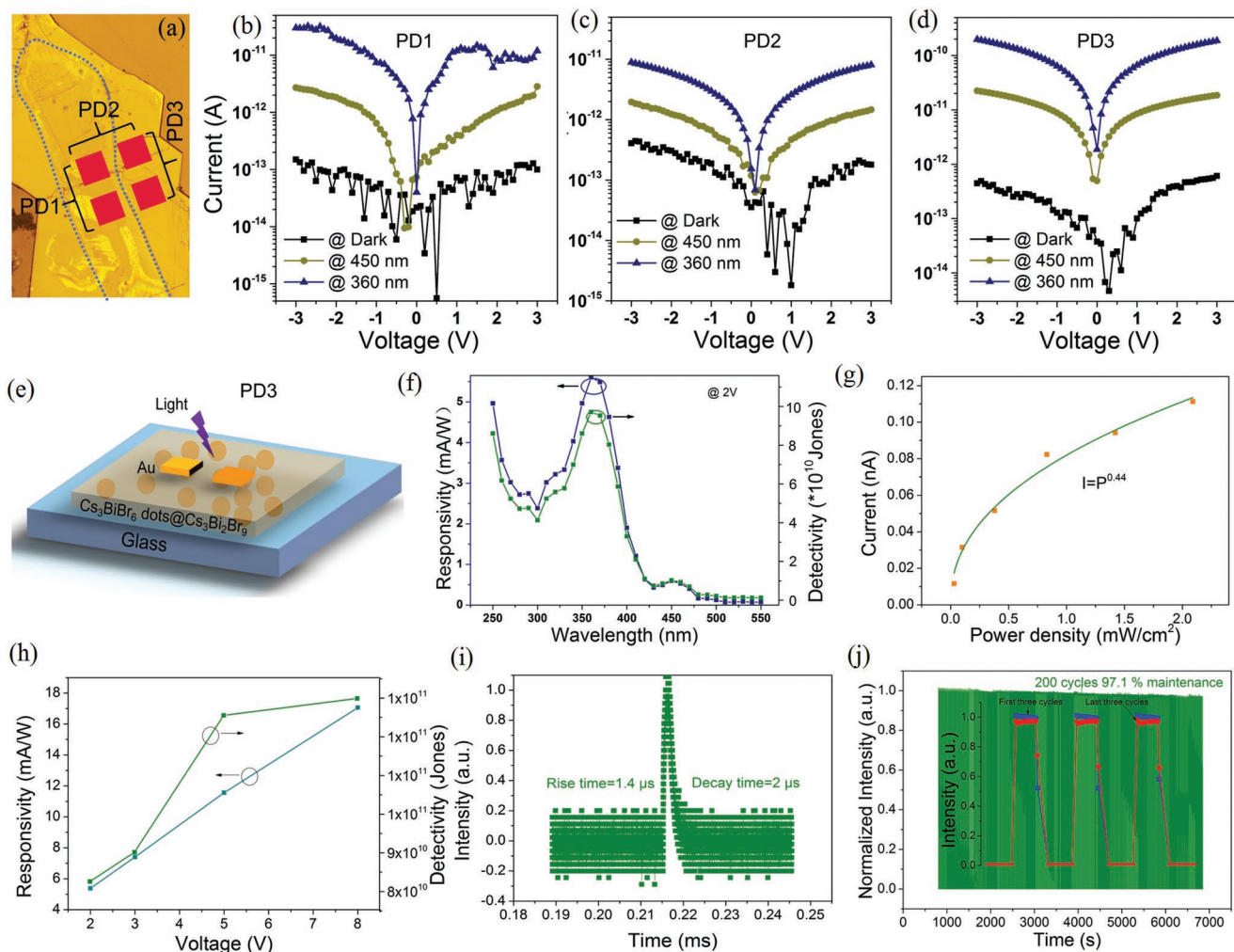
Figure 5. a) The structure of PD1, PD2 (Lateral heterojunction), and PD3 (Bulk heterojunction). b–d) The corresponding I–V curves of three PDs. e) Schematic diagram of PD3. f) The corresponding responsivity and detectivity spectra at 2 V bias. g) Photocurrent of the PD3 as a function of light intensity. h) Responsivity and detectivity as a function of bias (2.09 mW cm^{-2}; 360 nm light) i) Pulsed light response of the PD. j) I–t curves of the PD3 with 200 cycles and the inset is the corresponding first and last three cycles.

as proved by TEM. Figure 5e is the schematic diagram of the PD3. Figure 5f shows the responsivity[21,22] ($R = \dfrac{I_l - I_d}{PA}$, where I_l is the light current, I_d is the dark current, P is the power density, and A is the effective light area) and detectivity[23,24] ($D^* = \dfrac{R}{(2eI_d/A)^{1/2}}$, e = 1.6×10^{-19} C) spectra at 2 V bias of PD3, and the corresponding current time (I–t) curve is shown in Figure S8 (Supporting Information). The PD exhibits dual-band photodetecting performance with a UV main band (360 nm) peak R of 5.6 mA W^{-1} and a blue sub-band (450 nm) peak R of 0.6 mA W^{-1} at 2 V, and the corresponding D^* are 8.5×10^{10} Jones and 1.0×10^{10} Jones, respectively. The changing trends of R and D^* are in accordance with the absorption spectrum shown in Figure S9 (Supporting Information). And the calculated on–off ratios are 1.6×10^3 and 1.8×10^2 when illuminated by UV and blue light (Figure S10, Supporting Information). The high dual-band photodetecting abilities of PD3 shows great application prospect in light communication. The

corresponding dependence of photocurrent on light intensity[25] ($I_l = P^\theta$) is shown in Figure 5g and Figure S11 (Supporting Information). The value of θ is calculated as 0.44 for PD3. Figure 5h shows the R and D^* under different applied voltages (360 nm; 2.09 mW cm^{-2}) and Figure S12 (Supporting Information) is the corresponding I–t curves. Clearly, both R and D^* of the PD3 increase with the increase of the applied voltage, and the highest R and D^* are calculated as 16.5 mA W^{-1} and 1×10^{11} Jones, respectively, when 8 V bias is applied. Additionally, the linear dynamic range ($LDR = 20 \log \dfrac{P_H}{P_l}$, where P_H and P_L are the upper and lower limit of the incident light intensities and the photocurrent begins to deviate from linearity beyond this range) is also important merit for a PD,[12] and the result is shown in Figure S13 (Supporting Information). The LDRs at 360 and 450 nm are >36.9 and >34.2 dB, respectively.

Fast response speed to light signals is crucial to high-performance PDs. Figure 5i shows the pulsed light response of PD3, and Figure S14 (Supporting Information) shows the photoresponse

**ADVANCED
SCIENCE NEWS**

www.advancedsciencenews.com

**ADVANCED
FUNCTIONAL
MATERIALS**

www.afm-journal.de

measurement system. The PD exhibits state-of-the-art response speed with a rise time of 1.4 µs and decay time of 2.0 µs. Stability is another significant parameter for perovskite PDs. To determine the stability performance of the as-prepared CBB photodetectors, we investigated the stability under continuous UV illumination with a 365 nm UV lamp. The PD3 maintained 97.1% photodetection ability after 200 cycles of continuous measurement, as shown in Figure 5j, and the PD remained 91% of the photocurrent after 3 months (Figure S15, Supporting Information), demonstrating its good stability, which is comparable to the recent reported $Cs_2AgBiBr_6$ PD, respectively.[26]

The Mulliken electronegativity theory for atoms was used to calculate the flat-band potentials of semiconductors ($\chi = \dfrac{I + A}{2}$; where χ is the electronegativity of atoms, I and A represents first ionization energy and electron affinity, respectively.) as follows[27]: $E_{CB} = \chi_p - E^e - 1/2E_{g1}$ and $E_{VB} = E_{CB} + E_{g1}$, in which E_{CB} and E_{VB} are the positions of valence band maximum (VBM) and conduction band minimum (CBM), respectively; χ_p is the electronegativity and can be estimated by the geometric mean of the electronegativity of the constituent atoms; E^e represents the energy of free electrons on the hydrogen scale ($\approx$4.5 eV) and E_{g1} is the energy bandgap.[28] The calculated results for $Cs_3Bi_2Br_9$ and Cs_3BiBr_6 are summarized in Tables S1 and S2 (Supporting Information). A staggered type-II band alignment formed between $Cs_3Bi_2Br_9$ and Cs_3BiBr_6 as schemed in Figure S16a (Supporting Information) and the Fermi level of CBB is determined by Scanning Kelvin Probe Force Microscope

(SKPFM) measurements shown in Figure S17 (Supporting Information).[28] Based on the experimental phenomena, we illustrated the carrier generation and extraction process under 360 and 450 nm light irradiation, respectively. When the PD was illuminated by monochromatic visible light (450 nm, Figure S16b, Supporting Information), only the electrons at the valence band (VB) of $Cs_3Bi_2Br_9$ were excited to the conduction band (CB), and the holes generated at the VB will be transmitted to the VB of Cs_3BiBr_6. The electrons and holes will be collected by the electrode under applied bias (Figure S16d, Supporting Information). Carriers were generated in both of $Cs_3Bi_2Br_9$ and Cs_3BiBr_6 when the PD is illuminated by monochromatic UV–light (360 nm, Figure S16c,e, Supporting Information). Compared to the PD illuminated by 450 nm light, more electron and hole pairs were generated under the irradiation of 360 nm light (1. Carriers generated in $Cs_3Bi_2Br_9$. 2. Carriers separated by the heterojunction. 3. Carriers generated in Cs_3BiBr_6.), leading to its high responsivity.

The photocurrent signals could be regulated by the wavelength of incident light. The PD as the receiving terminal of the optical signal could output different photocurrent states under UV, blue or mixed light (UV and blue). When the PD was illuminated by 365 nm (0.24 mW cm^{-2}), 450 nm (2.05 mW cm^{-2}), or mixed light, the output electrical signals were defined as "**10**", "**01**", and "**11**", respectively, and the "**00**" signals were obtained in the dark condition (**Figure 6**a). A series of changing light signals were illuminated on the PD, resulting in the electrical signals shown in Figure 6b, in which the current of $\approx$100 pA is denoted "**11**", the current of $\approx$50 pA is defined "**10**", the current
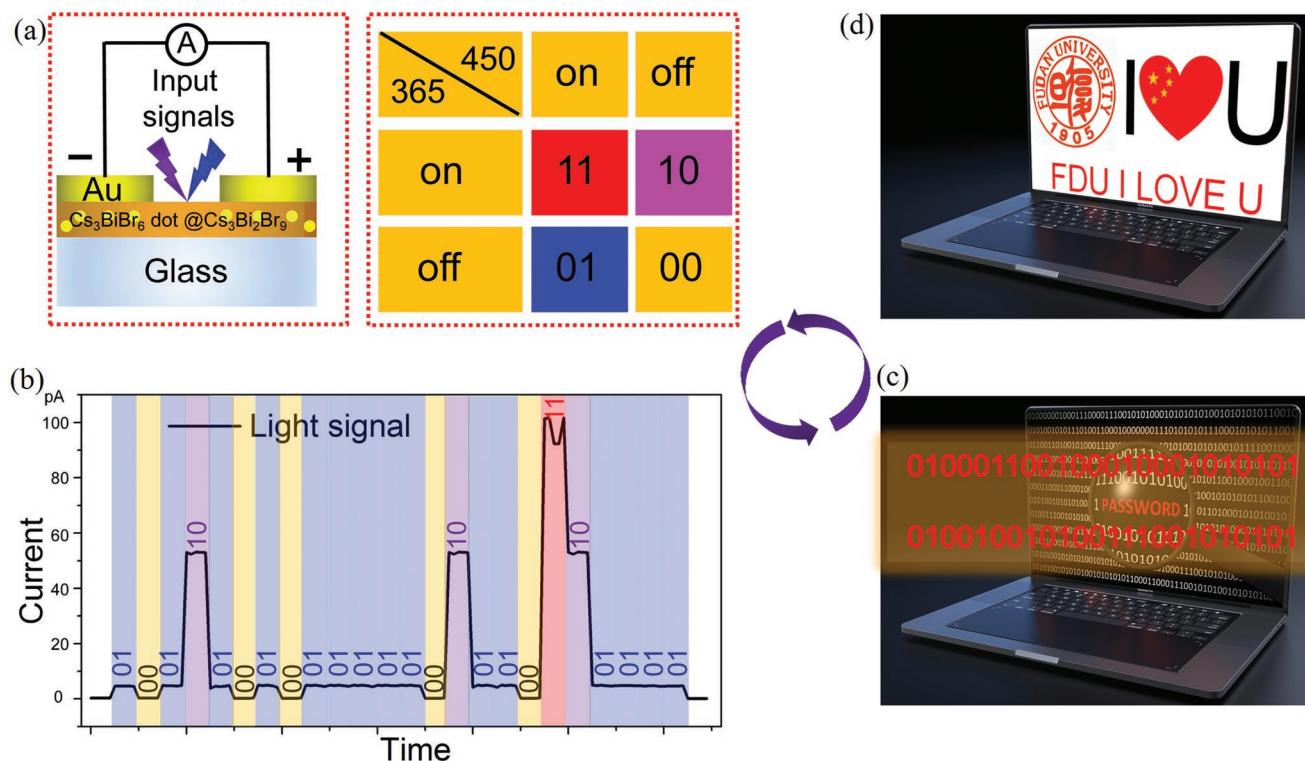
Figure 6. a) Schematic diagram of Cs_3BiBr_6/$Cs_3Bi_2Br_9$ PD and the corresponding signal generated under different conditions. b) Light signals recorded by Keithley 4200. c,d) Decryption code and transmitted signal, respectively.

of ≈5 pA is denoted "**01**", and in the dark condition, the signals are defined "**00**". When decoding the current signals by binary "**0**" and "**1**" digital signals(Figure 6c),[11,29] the message "FDU I O U" was obtained (Figure 6d). The one-step preparation of perovskite bulk heterojunction dual-band PDs not only enables large-scale fabrication but also is more confidential in the field of communication than single-band UV detectors, showing great application prospects in the field of quantum communication in the future.

3. Conclusion

In summary, for the first time, we observed a novel air induced the formation of $Cs_3Bi_2Br_9/Cs_3BiBr_6$(CBB) bulk heterojunction and proposed a reasonable growth mechanism. Theoretical and experimental characterizations suggest $Cs_3Bi_2Br_9$ exhibits a more stable structure in air than that of Cs_3BiBr_6. The bulk heterojunction achieved a high-performance dual-band photodetecting performance with a UV main band (360 nm) peak responsivity of 5.6 mA W^{-1} and a blue sub-band (450 nm) peak responsivity of 0.6 mA W^{-1} at 2 V. Furthermore, the PD exhibits fast response speed (rise time 1.4 µs and decay time 2.0 µs) and good cyclic stability. Our state-of-the-art findings open a new way for the fabrication of novel dual-band high-performance PDs based on lead-free perovskite bulk-heterojunction, showing great application prospects in the field of quantum communication.

4. Experimental Section

Fabrication of $Cs_3Bi_2Br_9/Cs_3BiBr_6$ (CBB) on the substrates: The substrates (glass) with a size of 1.5 × 1.5 cm were sequentially cleaned with water and ethanol in the ultrasonic bath, and dried with nitrogen. Before the growth process, 0.32 g CsBr (AlfaAesar Co., Ltd.; 99.9%) and 0.45 g $BiBr_3$ (AlfaAesar Co., Ltd.; 99%) were mixed and dissolved in the 1 mL C_2H_6OS (DMSO; 99.7%) solvent to prepare the saturated solutions at room temperature. The precipitations were removed by a 0.4 µm needle PTFE filter. 1 µL saturated solution was transferred to the center of glass, which was covered by the target glass. The growth temperature was kept at 60 °C. The detailed fabrication process could be seen in Figure 1a and in the previous report.[18]

Characterization of CBB: X-ray diffractometer (XRD, Cu-Kα radiation source, λ = 0.15418 nm) was used for crystal phase determination. The size and morphology of the CBB were determined by optical microscopy (Olympus). The thickness of the CBB was conducted by Step Profiler. X-ray photoelectron spectra (XPS) pattern of the CBB were collected by X-ray photoelectron spectrometer (Thermo Fisher ESCALAB 250; Al Kα X-ray radiation). Raman measurement was carried out using a Raman microspectroscopy (excitation wavelength 532 nm). Focused-ion beam (FIB) measurement was conducted on FEI Strata 400S. Photoluminescence tests were conducted by FLS920 fluorescence spectrometer with a 320 nm He-Cd laser as excitation source. Transmission electron microscopy (TEM) measurement was performed on JOEL JEM-2100F.

Fabrication of Photodetectors: Commercially bought Ni grids (300 meshes, with square voids of 50 µm side length) were put on the substrates under an optical microscope. Au electrodes (≈50 nm) were next thermally evaporated onto the sample. After removing the Ni grids, square-shaped electrodes with ≈20 µm apart were successfully formed on the CBB micro-ribbons.

Photoelectric Measurements of the CBB-based Photodetectors: All the photodetector measurements were performed by using a standard four-probe station with a Keithley 4200S semiconductor analyzer coupled with a 450 W Xe lamp equipped with a monochromator as the light source. And the power densities were tested through a NOVA II power meter (OPHIR Photonics). Also, a 355 nm Q-switch Nd:YAG laser and the oscilloscope (Tektronix MSO/DPO5000) were used to record the transient photoresponse. A UV lamp (365 nm) controlled by an electromagnetic relay was self-constructed for continuous measurement. All tests were performed in ambient air.

Single Point Energy Calculation: The density functional theory (DFT) calculations were performed using a Castep module. A surface model was cleaved from this super cell to simulate the (001) surface of Cs_3BiBr_6 and $Cs_3Bi_2Br_9$. The generalized gradient approximation (GGA) method with Perdew-Burke-Ernzerhof (PBE) function was employed to describe the interactions between core and electrons. In the vertical direction, a vacuum layer of ≈10 Å in thickness was introduced for the surface. The force and energy convergence criteria were set to 0.03 eV $Å^{-1}$ and 10^{-5} eV, respectively. It makes Cs_3BiBr_6 and $Cs_3Bi_2Br_9$ in the DMSO, DMSO/air (O_2 and H_2O), and air atmosphere at 298 K, 10^5 Pa, and the above stable structures are got. Then, the environment was removed from Cs_3BiBr_6 and $Cs_3Bi_2Br_9$. The Cs_3BiBr_6 and $Cs_3Bi_2Br_9$ structures were retained.

Supporting Information

Supporting Information is available from the Wiley Online Library or from the author.

Conflict of Interest

The authors declare no conflict of interest.

Data Availability Statement

The data that support the findings of this study are available in the supplementary material of this article.

[1] Y. Lei, Y. Chen, R. Zhang, Y. Li, Q. Yan, S. Lee, Y. Yu, H. Tsai, W. Choi, K. Wang, Y. Luo, Y. Gu, X. Zheng, C. Wang, C. Wang, H. Hu, Y. Li, B. Qi, M. Lin, Z. Zhang, S. A. Dayeh, M. Pharr, D. P. Fenning, Y. H. Lo, J. Luo, K. Yang, J. Yoo, W. Nie, S. Xu, *Nature* **2020**, *583*, 790.

[2] J. Feng, C. Gong, H. Gao, W. Wen, Y. Gong, X. Jiang, B. Zhang, Y. Wu, Y. Wu, H. Fu, L. Jiang, X. Zhang, *Nat. Electron.* **2018**, *1*, 404.

[3] Z. Li, Z. Li, Z. Shi, X. S. Fang, *Adv. Funct. Mater.* **2020**, *30*, 2002634.

[4] a) X. Chen, W.-g. Lu, J. Tang, Y. Zhang, Y. Wang, G. D. Scholes, H. Zhong, *Nat. Photonics.* **2021**, *15*, 813; b) J. Wang, J. Li, S. Lan, C. Fang, H. Shen, Q. Xiong, D. Li, *ACS Nano* **2019**, *13*, 5473.

[5] C. Wu, B. Du, W. Luo, Y. Liu, T. Li, D. Wang, X. Guo, H. Ting, Z. Fang, S. Wang, Z. Chen, Y. Chen, L. Xiao, *Adv. Opt. Mater.* **2018**, *6*, 1800811.

[6] Z. Zheng, Q. Hu, H. Zhou, P. Luo, A. Nie, H. Zhu, L. Gan, F. Zhuge, Y. Ma, H. Song, T. Zhai, *Nanoscale Horiz.* **2019**, *4*, 1372.

[7] F. Fang, H. Li, S. Fang, B. Zhou, F. Huang, C. Ma, Y. Wan, S. Jiang, Y. Wang, B. Tian, Y. Shi, *Adv. Opt. Mater.* **2021**, *9*, 2001930.

[8] L. Li, H. Y. Chen, Z. Fang, X. Meng, C. Zuo, M. Lv, Y. Tian, Y. Fang, Z. Xiao, C. Shan, Z. Xiao, Z. Jin, G. Shen, L. Shen, L. Ding, *Adv. Mater.* **2020**, *32*, 1907257.

[9] L. Su, H. Chen, X. Xu, X. S. Fang, *Laser Photonics Rev.* **2017**, *11*, 1700222.

[10] D. You, C. Xu, J. Zhao, F. Qin, W. Zhang, R. Wang, Z. Shi, Q. Cui, *Adv. Opt. Mater.* **2019**, *7*, 1801522.

[11] Y. Bu, J. Xu, S. Shi, J. Chen, M. Li, Q. Zhang, P. Yang, J. Xu, X. Zhang, L. Kong, L. Li, *J. Mater. Chem. C* **2021**, *9*, 9203.

[12] a) C. Zhou, H. Lin, Q. He, L. Xu, M. Worku, M. Chaaban, S. Lee, X. Shi, M.-H. Du, B. Ma, *Mater. Sci. Eng. R* **2019**, *137*, 38; b) D. Shao, W. Zhu, G. Xin, X. Liu, T. Wang, S. Shi, J. Lian, S. Sawyer, *J. Mater. Chem. C* **2020**, *8*, 1819.

[13] F. Cao, L. Li, *Adv. Funct. Mater.* **2020**, *31*, 2008275.

[14] M. N. Tran, I. J. Cleveland, E. S. Aydil, *J. Mater. Chem. C* **2020**, *8*, 10456.

[15] H. Yang, T. Cai, E. Liu, K. Hills-Kimball, J. Gao, O. Chen, *Nano Res.* **2019**, *13*, 282.

[16] Y. Liu, Y. Gao, J. Zhi, R. Huang, W. Li, X. Huang, G. Yan, Z. Ji, W. Mai, *Nano Res.* **2021**, *15*, 1094.

[17] a) Y. Zhang, J. Yin, M. R. Parida, G. H. Ahmed, J. Pan, O. M. Bakr, J. L. Bredas, O. F. Mohammed, *J. Phys. Chem. Lett.* **2017**, *8*, 3173; b) L. Wu, H. Hu, Y. Xu, S. Jiang, M. Chen, Q. Zhong, D. Yang, Q. Liu, Y. Zhao, B. Sun, Q. Zhang, Y. Yin, *Nano Lett.* **2017**, *17*, 5799.

[18] Z. Q. Li, X. Liu, C. Zuo, W. Yang, X. S. Fang, *Adv. Mater.* **2021**, *33*, 2103010.

[19] Y. Tang, M. Liang, B. Chang, H. Sun, K. Zheng, T. Pullerits, Q. Chi, *J. Mater. Chem. C* **2019**, *7*, 3369.

[20] R. Kandel, G. Schatte, G. Cheng, C. Palmer, D. Beauchemin, P. L. Wang, *Inorg. Chem.* **2020**, *59*, 7049.

[21] F. Cao, L. Su, T. Yan, Z. Li, D. V. Shtansky, X. S. Fang, *Adv. Electron. Mater.* **2022**, *8*, 2101373.

[22] S. Y. Li, Y. Zhang, W. Yang, H. Liu, X. S. Fang, *Adv. Mater.* **2020**, *32*, 1905443.

[23] F. Cao, L. Jin, Y. Wu, X. Ji, *J. Alloy. Compd.* **2021**, *859*, 158383.

[24] F. Cao, Z. Pan, X. Ji, *J. Appl. Phys.* **2021**, *129*, 204503.

[25] L. Zheng, X. Deng, Y. Wang, J. Chen, X. S. Fang, L. Wang, X. Shi, H. Zheng, *Adv. Funct. Mater.* **2020**, *30*, 2001604.

[26] a) W. X. Ouyang, F. Teng, X. S. Fang, *Adv. Funct. Mater.* **2018**, *28*, 1707178; b) X. Zhang, X. Liu, B. Sun, H. Ye, C. He, L. Kong, *ACS Appl. Mater. Interfaces* **2021**, *13*, 35949.

[27] X. Meng, Z. Li, H. Zeng, J. Chen, Z. Zhang, *Appl. Catal. B-Environ.* **2017**, *210*, 160.

[28] a) W. X. Ouyang, F. Teng, M. Jiang, X. S. Fang, *Small* **2017**, *13*, 1702177; b) F. Cao, T. T. Yan, Z. Q. Li, L. M. Wu, X. S. Fang, *Adv. Opt. Mater.* **2022**, https://doi.org/10.1002/adom.202200786.

[29] X. Zhang, J. Li, W. Yang, B. Leng, P. Niu, X. Jiang, B. Liu, *ACS Appl. Mater. Interfaces* **2019**, *11*, 24459.